International Journal of Modern Physics B, Vol. 8, No. 17 (1994) 2327–2352

FOCUSING OF QUASI-TRANSVERSE MODES IN ZINC AT ULTRASONIC FREQUENCIES

KWANG YUL KIM*, ARTHUR. G. EVERY† and WOLFGANG SACHSE*

**Department of Theoretical and Applied Mechanics, Thurston Hall, Cornell University Ithaca, New York 14853, USA*

†Department of Physics, University of the Witwatersrand, Johannesburg PO WITS 2050, South Africa

Received 17 February 1994

The intense focusing of quasi-transverse (QT) modes along the symmetry axis of zinc is observed by various methods at ultrasonic frequencies. The focusing is associated with a conical point on the QT sheet of the ray surface, and thereby the phenomenon of external conical refraction. The observations have been made first, with pointlike longitudinal (L) and shear (S) piezoelectric transducers acting as acoustic source and detector; second, with a breaking capillary source with Heaviside time-dependence and a capacitive displacement detector at epicenter; and third, using a laser source and piezoelectric detector. The amplitudes of the signals observed by the piezoelectric sources and detectors in both time and frequency domains show intense focusing in the symmetry direction [0001], side-lobed by diffraction fringes caused by the interferences between collinear rays associated with different wave vectors **k**. A broadband capacitive displacement signal shows a very sharp deep minimum associated with the arrival of the conical rays, being consistent with the calculation of the dynamic Green's function and the theory of phonon focusing for the medium.

1. Introduction

The focusing of thermal phonons in elastically anisotropic crystals at liquid He temperature has been extensively investigated.[1–3] Ultrasound, the wavelength of which is several orders of magnitude greater than that of thermal phonons, propagates in a medium with much less scattering and attenuation even at room temperatures and recently several authors reported focusing of ultrasonic waves propagating both in metals and insulators at room temperatures.[4–11] As Maris predicted,[3] focusing patterns of harmonic or quasiharmonic signals at finite wavelengths are modulated by interference fringes, which were observed with source and detector at 15 MHz by Weaver, *et al.*[6,8] and at 392 MHz by Wesner, *et al.*[9] For the broadband signals observed, for example, with a capillary fracture source and a capacitive displacement detector,[12] interference fringes are less obvious, and it is observed that discontinuities and other forms of singularity in displacement at the arrival of various

PACS Nos.: 62.65.+k, 43.35.+d, 62.30.+d.

wave fronts including those of quasi-longitudinal (QL) and quasi-transverse (QT) modes are dominated by high frequency components. In the direction of focusing of a particular mode the associated singularity becomes very pronounced. Besides the interference phenomenon, there are other important differences between the observations of thermal phonons and ultrasound. While the detectors for thermal phonons such as bolometers and superconducting tunnel junctions are polarization insensitive, ultrasonic transducers are by and large polarization selective in their mode of excitation and detection. In ballistic phonon imaging what is probed is the energy flux of a heat pulse, a scalar quantity, whereas in ultrasonic experiments the probed variables, such as displacement, velocity, and acceleration are vector quantities that depend on the direction.

There is an abundance of experimental observations of the focusing of phonons and elastic waves in cubic media and also to a lesser extent in trigonal and tetragonal media. However, no experimental observations of focusing in hexagonal media had been investigated until quite recently, when we published a brief report of the intense focusing of QT modes in the symmetry direction [0001] of a hexagonal zinc crystal[7] oriented on the transversely isotropic basal plane. The focusing was observed at ultrasonic frequencies with three different methods: longitudinal (L) piezoelectric PZT source and L detector, focused laser beam source and PZT L detector, and capillary fracture source and capacitive displacement detector. Zinc displays an extraordinary singular and degenerate type of focusing. This focusing is concentrated in the vicinity of an isolated singular point caustic called the conical point located in the high symmetry direction and it is closely related with the phenomenon of *external conical refraction*. The condition on the elastic constants for the existence of this conical point is[13,14]

$$\frac{(C_{13}+C_{44})^2}{[C_{13}\,(C_{33}-C_{44})]} > 1\ . \tag{1}$$

The present paper is an expanded version of that brief report, augmented by additional observations made with the combination of PZT L source with shear (S) detector and PZT S source with S detector. Because of the anisotropic spread of wave normals associated with the different directivities of sources and detectors, interference effects at finite wavelengths, and transversely isotropic symmetry about the direction [0001], the observed focusing with the various configurations of PZT sources and detectors shows remarkably different patterns.

2. Theory

2.1. *Polarization field, slowness and ray surfaces, and phonon focusing in zinc*

In elastically anisotropic media the phase and group velocities and polarization vectors of elastic waves depend on the propagation direction. Moreover, phase

and group velocities are not collinear. These issues are treated extensively in the literatures.[13,15] The group or ray velocity $\mathbf{V}_g$ is obtained from the relation[13]

$$\mathbf{V}_g \equiv \nabla_{\mathbf{k}}\omega = \nabla_{\mathbf{n}}V_p = \frac{\nabla_{\mathbf{s}}S}{\mathbf{s}\cdot\nabla_{\mathbf{s}}S}\ , \tag{2}$$

where ω is the angular frequency, $\mathbf{k}$ the wave vector, $\mathbf{n} = \mathbf{k}/|\mathbf{k}|$ the wave normal, V_p the phase velocity, $\mathbf{s}$ the slowness defined as $\mathbf{n}/V_p$, and S the equation of the slowness surface. S can be written in the form

$$S = \det|C_{ijkl}s_j s_l - \rho\delta_{ik}| = 0\ , \tag{3}$$

where C_{ijkl} and ρ are the elastic stiffness tensor and density of a medium, respectively. Equation (2) indicates that the outward normal to the slowness surface at any point is the direction of the group or energy velocity of the corresponding mode.

The elastic tensor of a hexagonal or transversely isotropic medium including zinc is characterized by five elastic constants which on the basis of the Voigt contracted notation are: C_{11}, C_{33}, C_{44}, C_{12} and C_{13}, while $C_{66} = (C_{11} - C_{12})/2$. Kim and Sachse[12] on the basis of measured group velocity data in two principal directions have obtained the following values for the elastic constants of zinc: $C_{11} = 163.75$ GPa, $C_{33} = 62.93$ GPa, $C_{44} = 38.68$ GPa, $C_{12} = 36.28$ GPa, and $C_{13} = 52.48$ GPa. The density of zinc used for the calculation of the elastic constants was $7.134\,\mathrm{kg/m^3}$. These values of elastic constants of zinc satisfy the relation (1) for the existence for a cusp about the symmetry direction [0001].

Figure 1(a) shows the (010) section of the slowness surface of zinc, which consists of three sheets corresponding to the QL, pure transverse (PT), and QT modes. For simplification we compress the crystallographic notation [0001] used for a hexagonal crystal to [001] which is the appropriate notation for transversely isotropic media including some unidirectional fiber reinforced composite materials. For transversely isotropic zinc, all sections belonging to the [001] zone are identical and the (010) section is typical of them. The three-dimensional shapes of slowness and group velocity surfaces can be easily visualized by rotating the curves shown in Figs. 1(a) and (b) about the [001] symmetry axis. For a $\mathbf{k}$ along an arbitrary direction in a zonal section, one of the QT modes, say, the QT1 mode, becomes a PT mode that is shear horizontally (SH) polarized parallel to the basal plane (001) and normal to the zonal plane. Both the QL and QT2 modes are polarized in the sagittal plane identical to the zonal section. Hence, we simply denote QT1 and QT2 as PT and QT, respectively. The polarization directions of both QL and QT modes of zinc are graphically described in Musgrave's book.[13] For example the polarization direction of either QL or QT mode with the wave normal direction OQ_∞ in Fig. 1(a), where the normal to the QT slowness surface points in the symmetry direction [001], is approximately 45° inclined from the [001]-symmetry axis in the (010) zonal plane.

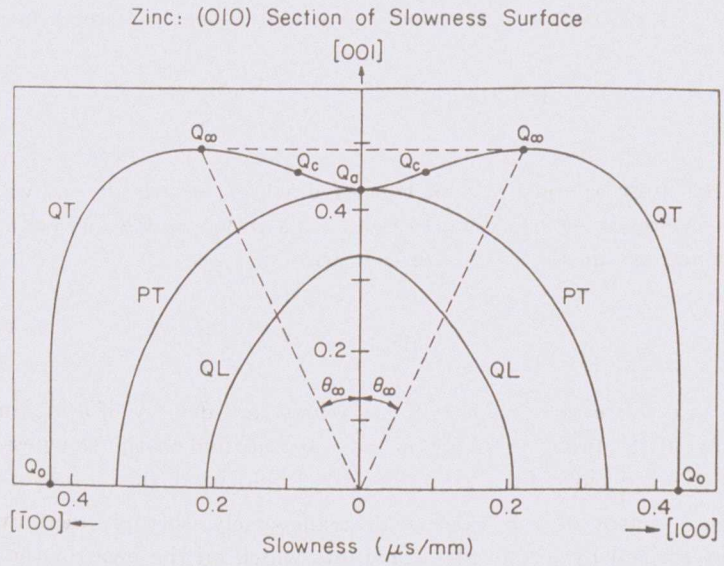

(a)

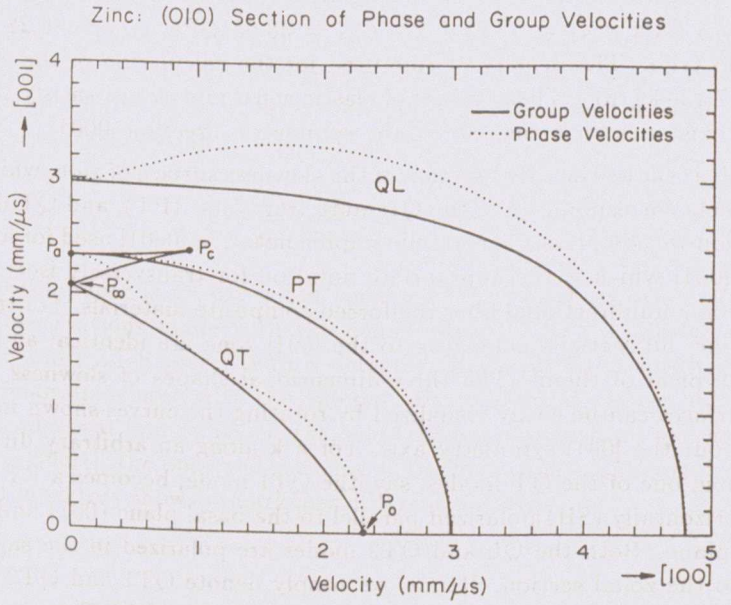

(b)

Fig. 1. (a) (010) section of the slowness surface in zinc. (b). (010) section of the group and phase velocity surfaces in zinc.

The group velocity (or ray) surface of zinc, obtained using Eq. (2), is drawn by the solid line in Fig. 1(b) together with the phase velocity surface which is depicted by the broken line for comparison. For zinc the QT wave propagates at a phase velocity less than that of the PT wave. For this reason the QT wave may be referred to as the slow transverse (ST) mode and the PT mode may be dubbed the fast transverse (FT) mode. However, for the group velocity surface in the cuspidal region, this distinction becomes somewhat blurred, as one can see that the QT sheet penetrates through the PT sheet. The cuspidal feature shown in Fig. 1(b) arises due to the particular shape of the QT mode slowness sheet shown in Fig. 1(a). Around the [001] axis it is concave with both the principal curvatures being negative. At point Q_c the principal curvature in the zonal section changes sign and the surface is saddle shaped from there to the point Q_∞, where the principal curvature transverse to the zonal plane changes sign. Beyond this point the QT slowness surface is convex. There is a circular band centered on the point Q_o where the slowness surface is again concave, leading to a tiny cuspidal feature around the point P_o. This cusp is not very well resolved in Fig. 1(b) because of its small size. None of the observations in this work is related to this region and we will not discuss it further. In Fig. 1(b) the points P_a and P_∞ on the symmetry axis, P_c on the cuspidal edge, and the point P_o on the basal plane correspond to the points Q_a, Q_∞, Q_c, and Q_o in Fig. 1(a). For simplicity of nomenclature, let us call the ray branches of the QT mode between P_a and P_c, P_c and P_∞, and P_∞ and P_o by the acronyms, FQT (fast QT) mode, IQT (intermediate QT) mode, and SQT (slow QT) mode, respectively. Note for reference that the directions of the cuspidal edge P_c on the ray surface and Q_c and Q_∞ on the slowness surface are oriented at 21.54°, 9.304°, and 24.52°, respectively, from the [001] symmetry axis.

Because of rotational symmetry about the [001] direction, the ray surface near P_∞ is conical in shape. The energy flux or group velocity associated with the point Q_∞ is parallel to the [001] symmetry direction as already mentioned. All the QT modes with their **k** vectors lying on the circular cone generated by rotating OQ_∞ about the [001] axis have the same ray vector located at the conical point P_∞ and have their acoustic energy directed along the symmetry direction [001]. This focusing of acoustic energy along the [001] symmetry direction is referred to as the *external conical refraction*[13] for the reason that when this single QT ray, OP_∞, impinges on the boundary between the hexagonal and an adjacent isotropic medium, the emerging family of rays in the isotropic medium on being refracted in accordance with Snell's law lies on the surface of a circular cone.

Because of the nonspherical shape of the slowness surface in anisotropic media, the ray vectors are more strongly clustered in some directions than in others, and this results in pronounced nonuniformity in the distribution of energy flux. The focusing of the QL and PT modes in zinc is not as significant as for the QT modes, because their sheets of the slowness surface are everywhere convex[13,16] and there is therefore no folding of the corresponding sheets of the wave surface (see Fig. 1(b)). In what follows we confine our attention to the QT modes which exhibit strong

focusing. A parameter that provides a good measure of focusing is the Maris phonon enhancement factor A defined as[17]

$$A \equiv \delta\Omega_s / \delta\Omega_v \tag{4}$$

where $\delta\Omega_s$ is the infinitesimal solid angle subtended by a small cluster of slowness vectors and $\delta\Omega_v$ is the infinitesimal solid angle subtended by their associated ray vectors. The enhancement factor A can be shown to be related to the Gaussian curvature $K = L_1 L_2$, where L_1 and L_2 are the two principal curvatures of the slowness surface; that is,

$$A = \frac{1}{(s^3 V_g |K|)} \,. \tag{5}$$

It follows from Eq. (5) that the lines of zero curvature on the slowness surface map onto caustics, where the energy flux is infinite.

Figure 2 shows the computed normalized focusing intensity $I(\theta)/I(1°)$ of QT waves at the top surface out to 15° from the [001] symmetry direction. It has been generated, assuming a uniform distribution of wave vectors **k** in all directions radiated from a point source at the origin on the bottom surface and using a Monte Carlo technique. The intense central peak (whose intensity is theoretically infinite) corresponds to the conical direction P_∞ in Fig. 1(b) and also to the circle of zero

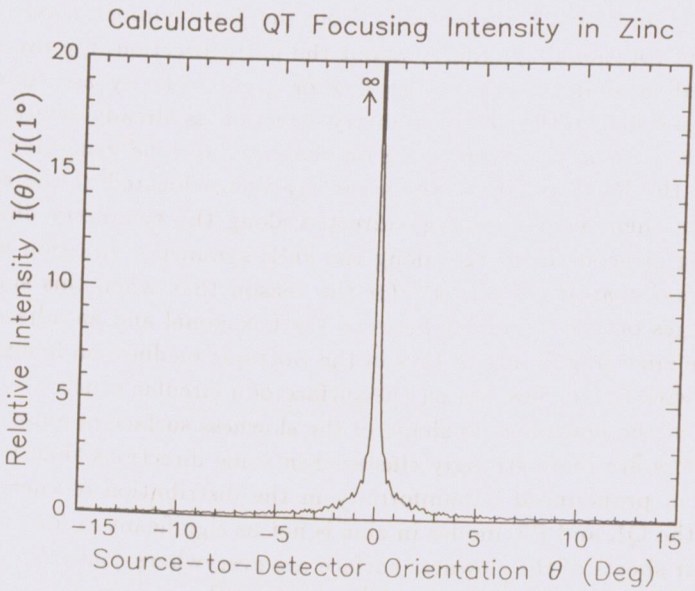

Fig. 2. Calculated QT mode focusing intensity $I(\theta)$ normalized with respect to $I(1°)$ in zinc.

Gaussian curvature on the slowness surface passing through the point Q_∞, on which A is infinite. Figure 2 shows how rapidly the QT acoustic intensity diminishes with increasing angular deviation from the symmetry axis.

Although individual caustics are well resolved in thermal phonon imaging,[1] in our experiment they are diffraction broadened because of the much larger characteristic wavelength. In simple terms the diffraction can be considered to arise from the interference of collinear harmonic or quasiharmonic rays associated with different **k**'s. An additional consideration is that the modes of excitation used in our experiments are either axisymmetric or shear horizontal, resulting in a generally nonuniform but smoothly varying distribution of wave normals in different directions. The striking consequences of these various source directivities are that some modes of vibration are more strongly excited in certain directions, while other vibrational modes are totally suppressed in all directions. The broadband ultrasonic signal generated by capillary fracture, the time function of which resembles a Heaviside step with a finite rise time,[18] exhibits a very intense and sharp pulse at the wave arrival in the direction of the caustics, a rounded version of the predicted singularity.[19] To delve further into this aspect we consider next the elastodynamic Green's function of zinc and its spatial and frequency dependence.

2.2. *Elastodynamic Green's functions*

Although the disk-shaped zinc specimen used in our experiment is finite in size, some salient features associated with an unbounded medium including ray arrivals and focusing are applicable to the specimen. In this section we recall some of the properties of the integral expressions for the frequency and time domain Green's functions of infinite anisotropic elastic continua, which we have recently reported.[11,19] Let $\tilde{G}_{sp}$ represent the s'th component of the displacement at point $\mathbf{x}$ and time t in response to a point force in the p'th direction with time dependence $F(t)$, applied at the origin. $\tilde{G}_{sp}$ and $F(t)$ are related by the Cauchy–Navier equation for an anisotropic medium:

$$\left(\rho\delta_{rs}\frac{\partial^2}{\partial t^2} - C_{rlsm}\frac{\partial^2}{\partial x_l \partial x_m}\right)\tilde{G}_{sp}(\mathbf{x}, t) = \delta_{rp}\,\delta(\mathbf{x})\,F(t)\ . \tag{6}$$

In the special case of $F(t)$ being the impulse function $\delta(t)$, $\tilde{G}_{sp}(\mathbf{x}, t)$ are the dynamic Green's functions $G_{sp}(\mathbf{x}, t)$. The array of $\tilde{G}_{sp}(\mathbf{x}, t)$ forms a tensor of second rank.

The formal solution to Eq. (6) in terms of integral transforms has been considered by many authors[20–25] and there have been several books and reviews written on the subject.[26–29] Of relevance to the experiments that will be described here are the frequency domain Green's functions

$$G_{sp}(\mathbf{x}, \omega) = \int G_{sp}(\mathbf{x}, t)\, e^{i\omega t}\, dt \tag{7}$$

and time domain response $\tilde{G}_{sp}(\mathbf{x}, t)$ to a concentrated force acting at the origin with Heaviside step function time dependence

$$F(t) = \Theta(t) = \begin{cases} 0, & t < 0 \\ 1, & t > 0 \end{cases} . \tag{8}$$

The latter is given in terms of the Green's function by

$$\tilde{G}_{sp}(\mathbf{x}, t) = \int G_{sp}(\mathbf{x}, \omega) f(\omega) e^{-\imath\omega t}\, d\omega \ , \tag{9}$$

where

$$f(\omega) = \frac{1}{2\pi} \int F(t)\, e^{\imath\omega t}\, dt \tag{10}$$

is the Fourier transform of the forcing function. We have shown in Refs. 11 and 19 that these are given by

$$G_{sp}(\mathbf{x}, \omega) = \sum_n \left\{ \frac{\imath\omega}{8\pi^2\rho} \int_\Omega d\Omega s^{(n)3} \Lambda_{sp}^{(n)}\, e^{\imath\omega\, \mathbf{s}^{(n)} \cdot \mathbf{x}} + \frac{1}{8\pi^2\rho x} \int_0^{2\pi} d\varphi\, s^{(n)2}\, \Lambda_{sp}^{(n)} \right\} \tag{11}$$

$$\tilde{G}_{sp}(\mathbf{x}, t) = \sum_n \left\{ \frac{-1}{8\pi^2\rho} \int_\Omega d\Omega s^{(n)3}\, \Lambda_{sp}^{(n)}\, \delta(t - \mathbf{s}^{(n)} \cdot \mathbf{x}) \right.$$
$$\left. + \frac{\Theta(t)}{8\pi^2\rho x} \int_0^{2\pi} d\varphi\, s^{(n)2}\, \Lambda_{sp}^{(n)} \right\} . \tag{12}$$

The index n appearing in these equations refers to the three different modes of particle vibration, i.e., longitudinal (L), fast transverse (FT), and slow transverse (ST); $s^{(n)}$ is the slowness defined as $1/V_p^{(n)}$, where $V_p^{(n)}$ is the phase velocity; $\Lambda_{sp}^{(n)} = U_s^{(n)} U_p^{(n)}$, where $\mathbf{U}^{(n)}$ is the polarization eigenvector associated with the eigenvalue $\rho V_p^{(n)2} k^2$ of the Christoffel tensor $\Gamma_{rs} = C_{rlsm} k_l k_m$; and $d\Omega$ is the element of solid angle for the slowness $\mathbf{s}^{(n)}$.

Equation (11) can be solved analytically for isotropic solids, leading to the results of Aki and Richards.[30] In the case of anisotropic solids, except for certain special cases where analytic results are known,[26,31] the angular integrals have to be performed numerically. At high frequencies the stationary phase approximation can be invoked, yielding a contribution to $G_{sp}(\mathbf{x}, \omega)$ of the form

$$G \approx \frac{\Lambda\, e^{\imath\omega\, \mathbf{s} \cdot \mathbf{x}}}{\sqrt{|K|}} \tag{13}$$

for each point on the slowness surface where the outward normal points in the observation direction. The intensity or energy flux associated with each contribution is proportional to $|G|^2$, and is thus inversely proportional to $|K|$, the magnitude of

the Gaussian curvature of the slowness surface. This is precisely what is predicted on the basis of the ray approximation as shown in Eq. (5).

The stationary values of $\mathbf{s} \cdot \mathbf{x}$ in Eq. (12) give rise to singularities in temporal variation of $\tilde{G}_{sp}(\mathbf{x}, t)$. These singularities propagate outwards from the source at group velocity $\mathbf{V}_g$ in any direction and are known as wave arrivals. There are many different singular forms these wave forms can take that include discontinuity, logarithmic divergence, kink (or discontinuity in slope), and inverse power-law divergence, depending on the curvature of the slowness and other factors.

Of particular interest to us is the singularity behavior of the Green's functions at and near the conical point P_∞ where the intense focusing of the QT mode in zinc occurs. The single ray OP_∞ corresponds to a circular cone OQ_∞ of the slowness surface, as described in Sec. 2.1. and thus constitutes a highly degenerate caustic. On the circular band between the Q_c and Q_∞ around the [001] symmetry axis the slowness surface is saddle-shaped or hyperbolic. Beyond Q_∞ and still near it the slowness surface of zinc is convex or elliptical. The condition for the existence of the conical point on the symmetry axis is given by the relation (1). The way the conical caustic evolves into a pattern of fold and cusp caustics when the symmetry lowered, has been described by Every.[32] The form of singularity at this conical point in the wave surface is discussed in the book of Payton[26] and is given by

$$\tilde{G}_{sp}(\mathbf{x}, t) \propto \begin{cases} 1/\sqrt{x|T|}\,; & T < 0 \\ 1/x\,; & T > 0 \end{cases}, \tag{14}$$

where T is measured from the arrival time of the singularity. Henceforth, the indices 1, 2, and 3 will denote the [100], [010], and [001] directions, respectively. From symmetry grounds, it is only the components $\tilde{G}_{11} = \tilde{G}_{22}$ and $\tilde{G}_{33}$ that are nonzero and display this singularity, and for the same reason $\tilde{G}_{13} = \tilde{G}_{23}$ vanishes to zero for $\mathbf{x}$ in the symmetry direction. Near to but not on the symmetry axis, where the symmetry is broken but there is still strong concentration of the wave normals of the QT mode (refer to Fig. 2), $\tilde{G}_{13} = \tilde{G}_{23}$ is expected to rise steeply. A little further away from the [001] direction, where the distribution density of QT-mode wave normals is drastically reduced (see Fig. 2), $\tilde{G}_{13}$ is then expected to fall precipitously. The $1/\sqrt{|T|}$ singularity and other singularities to be discussed later are expected to be preserved in both half-space and finite specimens. Figure 3 shows the results of Payton's calculation[26] of the normalized displacement along the symmetry direction in a half-space zinc specimen, expressed in units of $\rho F_3/(4\pi h C_{44})$ at a buried epicentral point due to a Heaviside step force acting on the surface in the same direction. Here ρ, F_3, and h represent the density, the magnitude of the Heaviside force, and the distance from the source to the detector, respectively. Note that the $1/\sqrt{|T|}$ singularity at the arrival of the conical ray is marked with the symbol $-\infty$ in the figure. This singularity in displacement amplitude is certainly caused by the intense focusing of the conical rays.

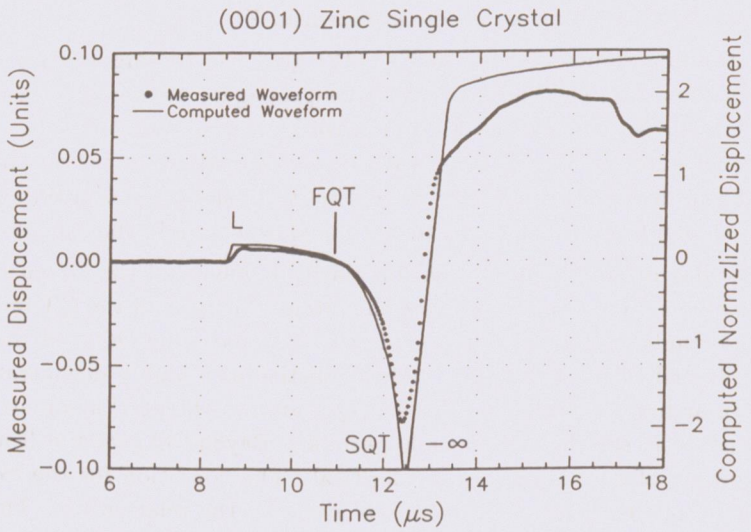

Fig. 3. Comparison between theoretical and observed epicentral displacements in a (0001) oriented zinc crystal.

The conical point in its immediate neighborhood resolves into the IQT and SQT branches in the ray surface. At the IQT wave arrival, which corresponds to the point in the saddle shaped region between Q_∞ and Q_c of the slowness surface, the displacement responses exhibit a logarithmic divergence. Similarly, at the SQT wave arrival very near the conical point, which corresponds to the convex region of the slowness surface just beyond Q_∞, there is a discontinuity in the Green's function. The arrival of the FQT ray that corresponds to the concave region between Q_a and Q_c of the slowness surface, causes a hardly noticeable kink in the Green's function $\tilde{G}_{33}$. The PT modes, being SH polarized, are not generated by the axisymmetric sources acting in the direction 3 parallel to the [001].

The consequence of these observations is that the peak amplitude in the observed Green's functions $\tilde{G}_{33}$, the square of which we use as a measure of intensity in a focusing profile, is found at the arrival of the conical ray in the symmetry direction, while a little further away from this direction the peak amplitude of both $\tilde{G}_{33}$ and $\tilde{G}_{13} = \tilde{G}_{23}$ is observed at the arrival of the IQT ray. In the neighborhood of the symmetry direction all the FQT, IQT, and SQT rays, which are associated with different $\mathbf{k}$'s on the slowness surface, arrive at the detector within a very short time interval of one another and at an ultrasonic frequency for finite wavelength, they interfere, causing diffraction fringes. For G_{33} and $G_{13} = G_{23}$, it is the interference of the IQT and SQT rays that dominate the diffraction fringes. Figures. 4(a) and (b) show the intensities of $|G_{33}|^2$ and $|G_{13}|^2$ at 2 MHz as a function of a source-to-detector angle θ measured from the symmetry direction.

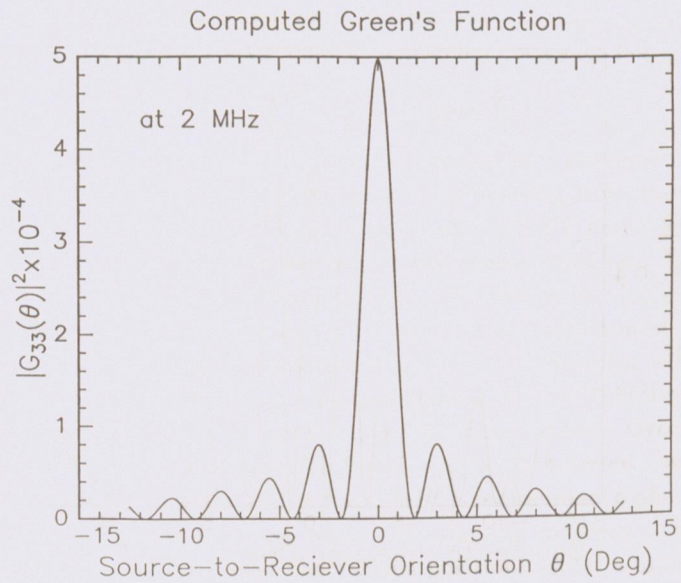

(a)

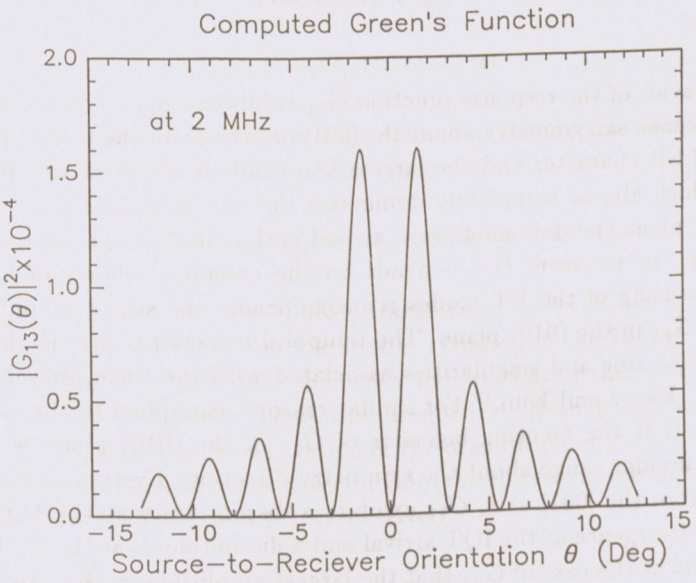

(b)

Fig. 4. Modulus of the frequency-domain Green's function as a function of the source-to-detector orientation: (a) $|G_{33}|^2$ at 2 MHz, (b) $|G_{13}|^2$ at 2 MHz, and (c) $|G_{11}|^2$ in the (010) plane at 3 MHz.

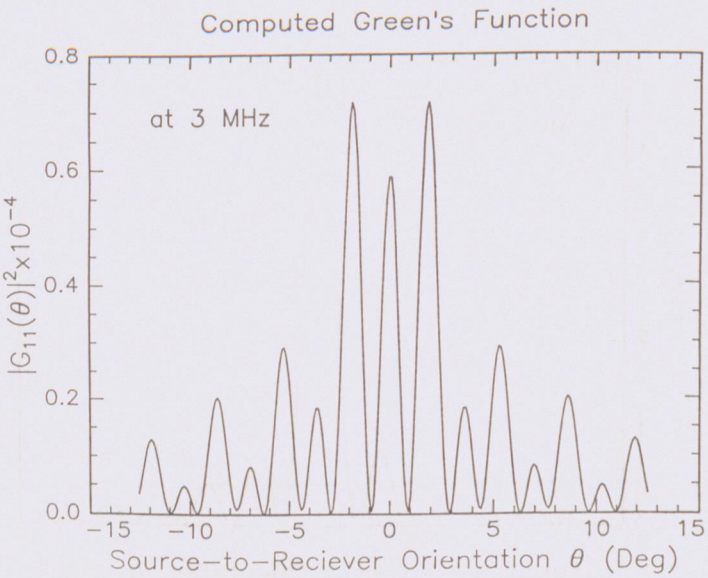

(c)

Fig. 4. (*Continued*)

The behavior of the response function $\tilde{G}_{11}$ exhibits a more complicated pattern because it breaks axisymmetry about the [001] direction. In the (100) plane the $\tilde{G}_{11}$ motion is of SH character and the largest amplitude is found at the arrival of the PT wave which almost completely dominates the $\tilde{G}_{11}$ in the far field. Conversely, in the (010) plane the dominant wave arrival is that of the IQT wave which is SV in character. In between, $\tilde{G}_{11}$ depends on the combined effects of both modes. Since the focusing of the PT modes is insignificant, our study is confined to the behavior of $\tilde{G}_{11}$ in the (010) plane. The temporal behavior of $\tilde{G}_{11}$ in the (100) and (010) planes of zinc and singularities associated with the wave arrivals have been described by Every and Kim.[19] For similar reasons as applied to the $\tilde{G}_{33}$ motions, one expects that the focusing behavior of $\tilde{G}_{11}$ in the (010) plane is confined in the narrow angular range about the symmetry direction. Every and Kim[19] showed that away from the [001] axis, $\tilde{G}_{11}$ exhibits a discontinuity at the FQT arrival, a logarithmic divergence at the IQT arrival and a discontinuity at the SQT arrival. It is expected as in the case of $\tilde{G}_{33}$ that the largest amplitude in $\tilde{G}_{11}$ can be found at the arrival of the conical and IQT rays in the symmetry and surrounding directions, respectively. Diffraction fringes at ultrasonic frequencies are in this case caused by the interference between all three QT modes: the FQT, IQT and SQT modes. The behavior of $|G_{11}|^2$ at 3 MHz in the (010) plane is displayed as a function of the source-to-detector orientation θ measured from the symmetry axis in Fig. 4(c).

In our experiment the L and shear (S) piezoelectric PZT sources act in the symmetry and horizontal directions, respectively, and they are scanned in position on the top surface of the specimen. The L and S PZT detectors, which sense displacements in the [001] and horizontal directions, respectively, are fixed at origin on the bottom surface of the specimen. The source acting on the top surface with the time function $F(t)$ appearing in Eq. (6) is modeled as a monopolar force and it is transmitted to the specimen through a coupling medium from the piezoelectric source transducer. The output voltage $V(\mathbf{x}, t)$ of the PZT detector corresponds to the surface displacement of the sample at the sensor location. The output of a L detector with a L source corresponds to the displacement $\tilde{G}_{33}(\mathbf{x}, t)$ while the output of a S detector with a L source corresponds to the horizontal displacement $\tilde{G}_{31}(\mathbf{x}, t) = \tilde{G}_{13}(\mathbf{x}, t)$. The output voltage $V(\mathbf{x}, t)$ of the S detector with a S source, with both S PZT transducers being polarized parallel to the [100] direction, corresponds to the horizontal displacement $\tilde{G}_{11}(\mathbf{x}, t)$. These various Green's functions are described in Eq. (9). The transfer function $T(\mathbf{x}, t)$ between the surface displacement and $V(\mathbf{x}, t)$ is a scalar function, which is assumed to be independent of the position $\mathbf{x}$. This is the case when the coupling between the sample and the scanning source is uniform over the various positions under a uniform pressure applied to the source transducer. This assumption is met reasonably well in our experiments which will be described in the next section. The sensor output voltage $V(\mathbf{x}, t)$ is then related to the surface displacement through a convolution integral

$$V(\mathbf{x}, t) = \tilde{G}_{sp}(\mathbf{x}, t) * T(t) \; . \tag{15}$$

Here $*$ denotes a convolution in the time domain. Taking the temporal Fourier transform of Eq. (15) with the help of Eq. (9) yields

$$v(\mathbf{x}, \omega) = f(\omega)\, \tau(\omega)\, G_{sp}(\mathbf{x}, \omega) \; , \quad \text{with } sp = 33,\ 13 \text{ or } 11 \tag{16}$$

where $v(\mathbf{x}, \omega)$ and $\tau(\omega)$ are the Fourier transforms of $V(\mathbf{x}, t)$ and $T(t)$, respectively. Equation (16) indicates that the spatial variation of the Fourier spectrum of the detector output at a particular frequency follows that of the Green's function, $G_{sp}(\mathbf{x}, \omega)$ with $sp = 33$, 13 or 11 at that frequency. Both $|G_{33}|^2$ and $|G_{13}|^2$ at 2 MHz, and $|G_{11}|^2$ at 3 MHz, as a function of the orientation angle $\theta = \tan^{-1}(x/h)$, where x denotes the distance of the detector from the epicentral symmetry direction, are shown in Figs. 4(a), (b), and (c), respectively.

3. Experimental Method

The zinc specimen used in our experiment is disk-shaped, 75 mm in diameter and 25.8 mm thick, and oriented in the [001] symmetry direction. It is prepared with both top and bottom planes polished and parallel to each other. The orientation in the [001] direction was achieved within 0.5° using an x ray diffraction pattern.

A finer adjustment of orientation within 0.25° was achieved by utilizing the symmetry property of the sound-wave propagation in the region around the [001] direction in zinc.

Figure 5 shows the geometric configuration of glass capillary fracture source and capacitive displacement transducer having a sensing element 1 mm in diameter. The capacitive transducer senses the displacement component normal to the surface and is fixed at the origin on the bottom surface. A tiny capillary less than 0.1 mm in diameter is laid on the 0.08 mm thick polyvinylidene fluoride (PVDF) film placed on top surface of the sample and broken at various positions. The elastic waves are generated by a sudden fracture of the capillary when it is pressed vertically down with a razor blade. This represents an axisymmetric source of vertical force drop whose time function resembles a Heaviside step with risetime less than 0.1 μs and excites only QL and QT modes propagating in the planes belonging to the [001] zone. The magnitude of force drop at the time of the capillary fracture is measured via a miniature load cell attached to the razor blade and ranges typically from 5 N to 10 N. The group velocity data associated with the QL, FQT, IQT, and SQT ray branches in Fig. 1(b) have been obtained from the wave forms detected by the capacitive transducer. The miniature capacitive transducer used in this experiment has been described by Kim *et al.*[33] Signals detected by the capacitive transducer are amplified by a charge amplifier whose bandwidth extends from 10 kHz to 10 MHz and the voltage-to-charge sensitivity of which is 0.25 V/pC. The output of the charge amplifier is connected to a digitizer where it is sampled at a 60 MHz rate with 10 bit resolution and the digitized signal is displayed on a x–y oscilloscope for visual observation. The output of the PVDF film generated at the instant of capillary fracture, serves as a trigger to the digitizer and also indicates the time of source

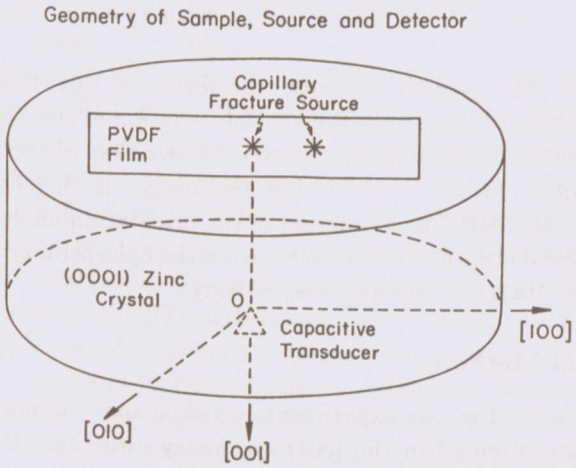

Fig. 5. Geometric schematic of capillary fracture source and capacitive displacement transducer.

excitation that provides a reference time for measurements of travel times of various rays propagating from the source to the detector. All these signals are stored on the hard disk of a microcomputer for subsequent data analysis and signal processing.

Shown in Fig. 6 is a schematic of the specimen showing the acoustic sources which were scanned across the epicentral position on the top surface and the piezoelectric PZT detectors that were fixed at origin on the bottom surface. The acoustic sources included not only axisymmetric sources, such as the pulsed excitation of a L PZT transducer and the irradiation of a pulsed, focused laser beam, but also the nonaxisymmetric excitation of a S PZT transducer. Four combinations of source and detector correspond to Fig. 6: (i) a L PZT source and a L PZT detector, (ii) a L PZT source and a S PZT detector, (iii) a S PZT source and a S PZT detector, both of which are polarized in the same direction, and (iv) a laser source and a L PZT detector. The S PZT source in (iii) was scanned in the direction of its polarization. The size of all the PZT sources and detectors were 0.75 mm in diameter except for the L PZT detector that was used with the laser source, which was 1.3 mm in diameter. Laser pulses, 4 ns in duration, were obtained from a Q-switched (Nd:YAG) laser that was focused into a spot size less than 0.5 mm in diameter. The piezoelectric sources were excited by a high voltage pulse derived from Panametrics, Model 5055PR. The elastic pulses generated by the piezoelectric and laser sources propagated through the specimen and were detected by the PZT transducers whose outputs were amplified by 60 db using a low-noise preamplifier whose −3db bandwidth nominally extended from 20 kHZ to 2 MHz. The actual high frequency cutoff of this amplifier was well beyond 10 MHz. As in the case of the capillary fracture source and capacitive transducer, the amplified signals were digitized and processed similarly in a microcomputer.

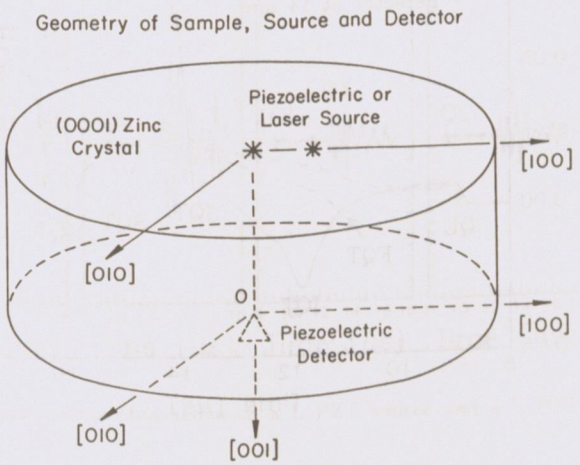

Fig. 6. Geometric schematic of PZT and laser sources and PZT detectors.

4. Results and Discussion

An epicentral displacement signal obtained with the system of capillary fracture and capacitive transducer is plotted in Fig. 3, which also shows for comparison Payton's theoretical displacement curve for a half-spaced zinc specimen. The arrivals of L, FQT, and SQT rays are indicated in the figure. Note the close similarity between the two waveforms in Fig. 3. The discrepancies between the two waveforms after 16 μs results from the presence of reflected signals from the side walls of the finite-sized specimen in the observed signal. Payton's calculation predicts a discontinuity at the L wave arrival, a change in slope or a kink at the FQT arrival and a negative square root singularity at the SQT arrival. The singularity is the result of the strong focusing of QT modes at the conical point in zinc and agrees well with the implication of the infinite phonon focusing factor shown in Fig. 2. The measured epicentral waveform in Fig. 3 clearly exhibits a deep negative minimum at the time of the SQT arrival. The fact that it is finite is due to the finite aperture of the source and detector and the finite bandwidth of the source-generation and wave-detection systems. It is noted that the observed behavior associated with the finite minimum is well accounted for when the theoretical Green's function is convolved with a linear ramp-step function with risetime of 0.1 μs, which closely approximates the time function of the capillary fracture source. Away from the symmetry direction, the negative square root singularity is weakened to a logarithmic divergence, which follows the IQT branch (see in Fig. 7, for example, the signal detected at 5 mm

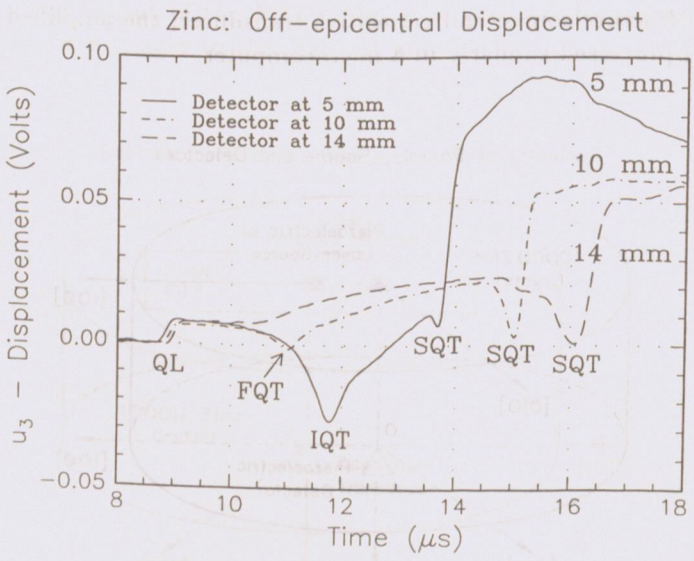

Fig. 7. Off-epicentral displacement signals near the symmetry direction, which are detected by a capacitive transducer.

for which $\theta = 10.97°$). The 10 mm detector position ($\theta = 21.19°$) in Fig. 7 roughly corresponds to the cuspidal edge which is at $\theta = 21.54°$. The signals shown in Fig. 7 exhibit a second minimum which is initally small but for larger source-receiver separations grows in magnitude. It is associated with the arrival of the head wave which slightly precedes the arrival of the SQT ray. The evolution of the waveform with increasing θ and changes that occur as the cuspidal edge is crossed, have previously been described by Kim and Sachse[34] and Weaver, *et al.*[35] Note in Fig. 7 the absence of the PT mode as is expected with the axisymmetric capillary fracture source.

The signals generated by the L PZT source and detected by the L PZT transducer are displayed in Fig. 8. The square of the peak amplitude immediately following the arrival of the QT mode is used as a measure of intensity. The angular variation of the corresponding QT mode intensity normalized against that in the symmetry direction is shown in Fig. 9. The QT mode focusing patterns obtained similarly with the L PZT source and the S PZT detector, the S PZT source and the S PZT detector, and laser source and the L PZT detector are shown in Figs. 10, 11, and 12, respectively. Figures 9–12 indicate that strong focusing is confined within an angle of about 1° of the symmetry direction. This is remarkable, considering the various factors that contribute to the widening of the focal region, including the finite aperture of the source and detector and the finite bandwidth of the wave generation and detection system.

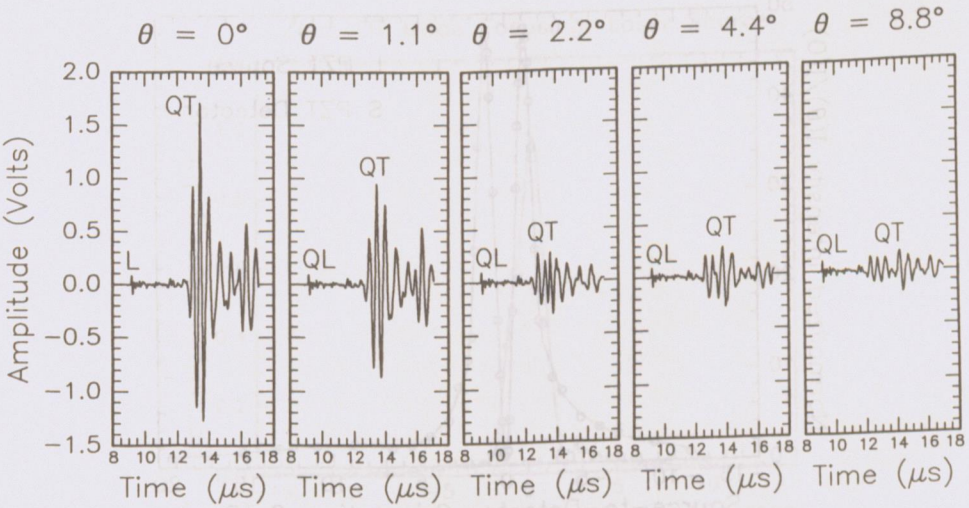

Fig. 8. Observed wave forms obtained with a L PZT source and a L PZT detector near the symmetry direction.

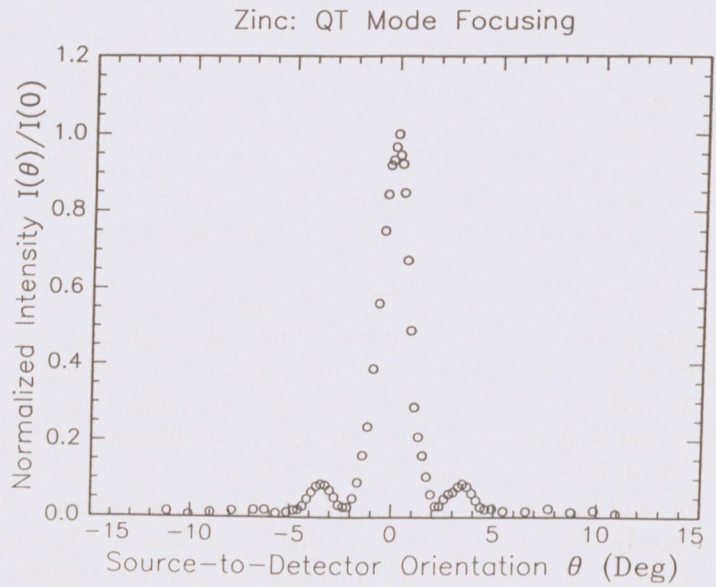

Fig. 9. Observed QT mode focusing pattern with a L PZT source and a L PZT detector.

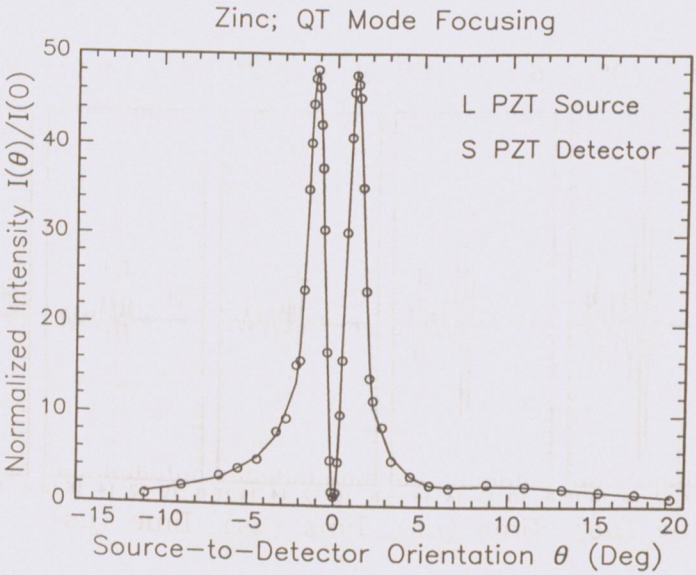

Fig. 10. Observed QT mode focusing pattern obtained with a L PZT source and a S PZT detector.

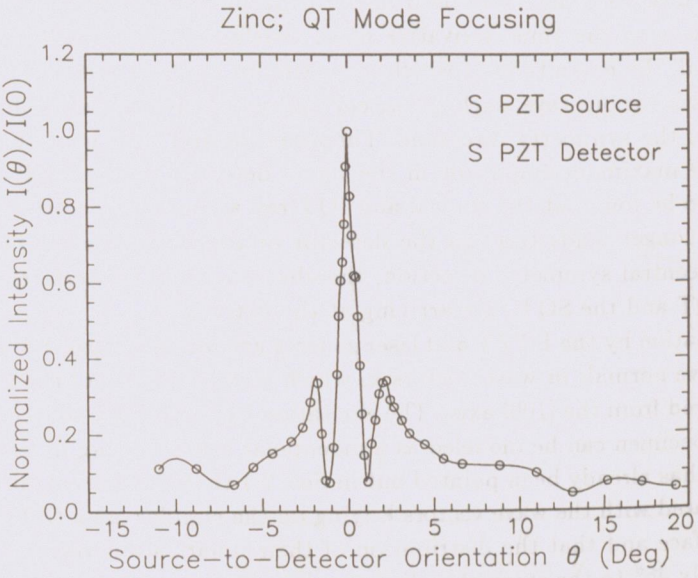

Fig. 11. Observed QT mode focusing pattern obtained with a S PZT source and a S PZT detector, both of which were polarized in the same direction in the sagittal plane.

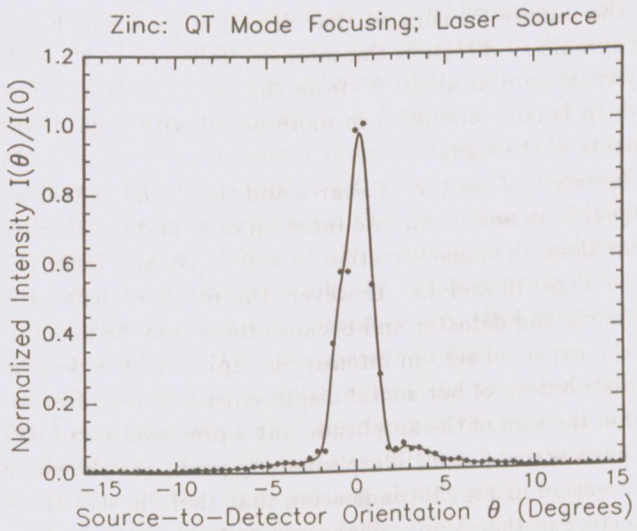

Fig. 12. Observed QT mode focusing pattern obtained using a laser source and a L PZT detector.

The thin disk PZT detectors used in our experiments are observed to be principally sensitive to the time derivative of the surface displacement signal or the velocity signal, the magnitude of which is maximum at the arrivals of singularities associated with various rays, such as the conical ray in the symmetry direction and IQT ray near the symmetry direction. Therefore, in and very near the epicentral direction, the maximum amplitude in the signal detected by the PZT transducers is expected to be found at the conical and IQT ray arrivals, respectively. However, this may no longer holds true, as the detector or the source moves further away from the epicentral symmetry direction, thereby causing the interference between the FQT, IQT and the SQT rays arriving at the detector.

The excitation by the L PZT and laser sources generates an axisymmetric distribution of wave normals or wave vectors $\mathbf{k}$, which is independent of the longitudinal angle measured from the [100] axis. The excitation by the L PZT source on the surface of the specimen can be modeled as a monopolar source acting in the symmetry direction. It has already been pointed out in Sec. 2.1 that the epicentral QT conical ray is associated with the wave vectors $\mathbf{k}$ lying on the circular cone OQ_∞ of the QT slowness surface and that the distribution of their polarization vectors inclined at approximately 45° to the symmetry direction is axisymmetric about the [001] axis. The displacement vectors for these conical wave vectors $\mathbf{k}$ with their energy flux pointing in the symmetry direction superpose constructively along the symmetry direction, while in the horizontal direction they cancel completely, resulting in a net displacement along the [001] symmetry direction. The constructive superposition of the displacements of these conical $\mathbf{k}$ wave vectors along the symmetry direction is evidenced in the intense focusing in that direction shown in Figs. 9, 11 and 12. Away from the symmetry direction the intensity falls off very rapidly. There is a small secondary maximum at about 3° from the axial direction. This is the result of diffraction which is later discussed in more detail with regard to the individual Fourier components of the signal.

For the configuration of the L PZT source and the S PZT detector the horizontal displacement signal is an antisymmetric function of θ, and the intensity is therefore theoretically zero along the axial direction ($\theta = 0°$). By and large this is confirmed experimentally in Figs. 10 and 13. However, the measurements are made with a finite aperture source and detector and because there may be a slight misalignment between them, the expected zero in intensity is replaced by a deep minimum. The antisymmetric distribution of horizontal displacements is manifest in Fig. 13 which shows a reversal in the sign of the amplitude but a preservation of its magnitude for measurements taken across $\theta = 0$. Sharp intensity peaks are shown on both sides of the symmetry direction in Fig. 10, indicating that there is still the strong concentration of ray vectors in the vicinity of the symmetry axis as discussed in Sec. 2.2. Recall that there is no focusing in an isotropic solid. The strong concentration of the near-conical wave normals in zinc may be further supported by the absence of the corresponding sharp intensity profiles in a similarly obtained curve using an isotropic specimen such as a glass plate. The intensity curve of the isotropic

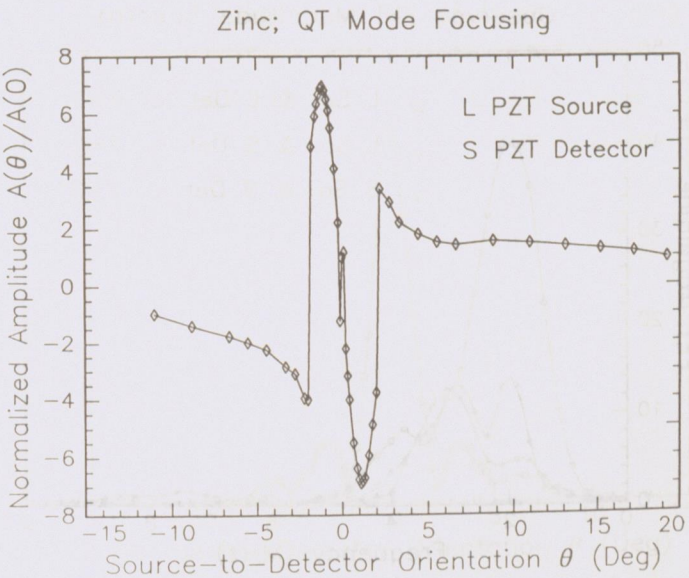

Fig. 13. Observed QT mode peak amplitude pattern obtained with a L PZT source and a S PZT detector.

specimen shows a very low intensity profile in the near-epicentral direction in an overall smoothly varying pattern observed in a wide range of source-to-detector orientation angles θ. The radiation patterns observed in an isotropic solid with various configurations of point-source and point-detector will be reported elsewhere.

The excitation by the S PZT source on the sample surface is modeled as a monopolar force acting in a horizontal direction, generating a non-axisymmetric distribution of wave vectors $\mathbf{k}$. Applying the reciprocity theorem of the Green's functions leads to the converse argument, that is, the axial displacements for the conical wave vectors $\mathbf{k}$ interfere destructively, resulting in the net displacement being zero along the symmetry direction, while the displacements along the horizontal direction in the zonal plane superpose constructively, thus exhibiting high intensity along the symmetry direction. This is apparent in Fig. 11.

Figures 9, 10 and 11 and to a lesser extent the laser-generated result shown in Fig. 12 exhibit a certain degree of interference behavior characterized by the secondary maxima and minima. To investigate these phenomena further, we take the Fourier transforms of the time-domain signals used to generate Figs. 9–11. Typical examples of these Fourier magnitude spectra are shown in Fig. 14. To obtain these, a time window has been used on the waveforms to analyze only the QT mode signals that arrive directly from the source. The Fourier spectra of all the observed signals corresponding to Figs. 9 and 10 with the L PZT sources, possess a broad peak centered at 2 MHz and those of the S PZT source and the S PZT

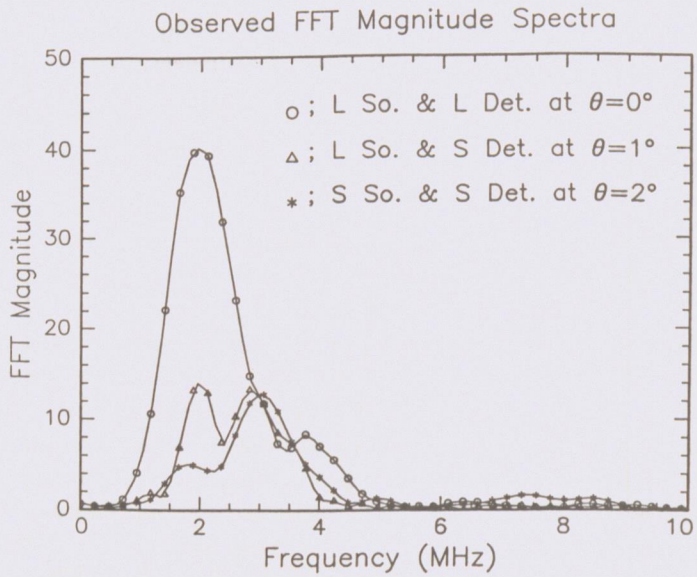

Fig. 14. Fourier magnitude spectra of the typical signals used to generate Figs. 9–11.

detector corresponding to Fig. 11 have a broad peak that is centered at 3 MHz. We also note that those of the L source and the S detector have a second broad peak appearing around 3 MHz. These results are consistent with Eq. (16), provided that the frequency profile of $G_{sp}(\mathbf{x}, \omega)$ is a slowly varying function of $\mathbf{x}$ in the ultrasonic frequency range at all the detector positions. The frequency spectrum of $G_{sp}(\mathbf{x}, \omega)$ at a particular position $\mathbf{x}$ is entirely due to the impulse source acting at the origin.

From the Fourier magnitude spectrum for each observed signal, the squared modulus of the peak amplitude at 2 or 3 MHz is plotted as a function of the source-to-detector orientation angle θ. Figures 15(a), (b) and (c), which correspond respectively to the signals shown in Figs. 9, 10 and 11, show the behavior of this intensity. A comparison of Figs. 15(a), (b) and (c) with the corresponding computed graph in Fig. 4 show that the observed Fourier spectra of the signals detected at various positions are in good agreement with the theoretically calculated curves with regard to the widths and positions of the central second and third maxima and minima. The absence of higher-order fringes in the observed Fourier spectra is expected, since the frequency spectra of the observed signals are fairly broadband centered around 2 or 3 MHz and low intensity, higher-order side fringes disappear as a result of the interference of broadband frequency components. As explained in Sec. 2.2, the fringes of Figs. 15(a) and (b) principally arise as a consequence of the interference between the IQT and the SQT modes arriving at the detector while the fringes shown in Fig. 15(c) are the result of an interference between all the transverse branches arriving at the detector.

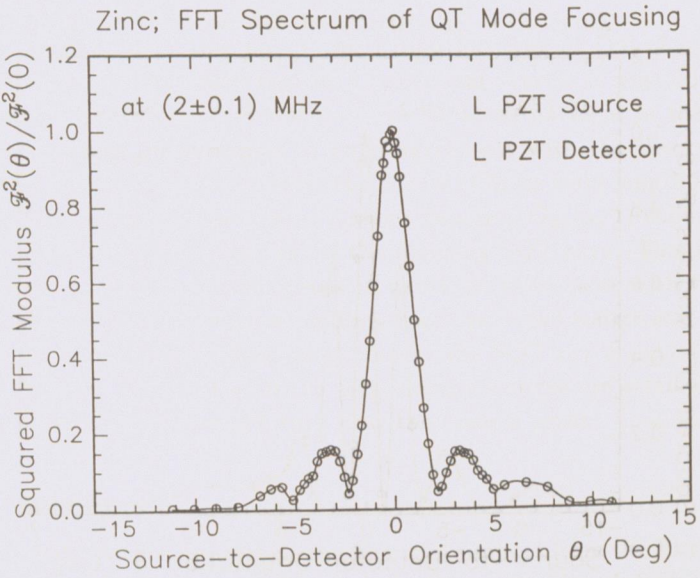

Fig. 15. Variations of the observed Fourier intensities as a function of source/receiver orientation θ: (a) with a L PZT source and a L PZT detector at 2 MHz; (b) with a L PZT source and a S PZT detector at 2 MHz; (c) with a S PZT source and a S PZT detector at 3 MHz.

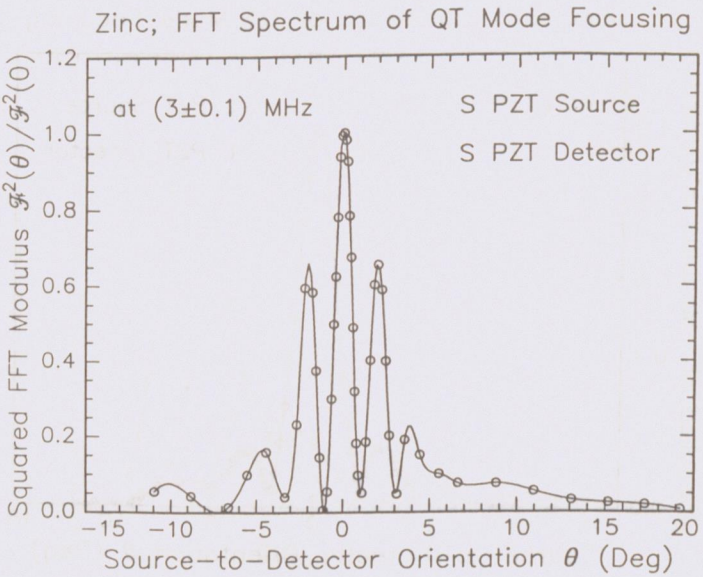

(c)

Fig. 15. (*Continued*)

The sound source associated with the impact of a relatively weak pulsed laser beam interacting with the specimen in the thermoelastic regime can be modeled as a pair of force dipoles aligned transversely in the horizontal radial direction.[36] However, when the intensity of the laser beam is high enough to cause ablation of the specimen surface, the source is modeled as a monopolar force acting in the symmetry direction with weak radial dipole component.[36] In our experiments, the laser source falls in the latter category with its focusing pattern shown in Fig. 12 resembling that shown in Fig. 9, which was obtained with a L PZT source and a L PZT detector. The analysis of the Green's functions associated with the laser source acting on zinc lies beyond the scope of this investigation.

It is emphasized that the intensity patterns obtained with the various configurations of source and detector include the combined effect not only of focusing and diffraction but also of the more smoothly varying anisotropic distribution of wave normals resulting from the directivities of the source and detector. All of these effects are included in the calculation of the Green's function. Because of the rather complicated mapping between $\mathbf{k}$ and $\mathbf{V}_g$ spaces, however, the effects of surface directivity is not easily separated from the other effects. For an axisymmetric excitation there is very little radiation of QT-mode $\mathbf{k}$'s along the symmetry direction. The most striking consequence of this is seen in Fig. 3 by the barely perceptible feature at the arrival of the FQT signal.

5. Conclusions

We have demonstrated in this paper the strong focusing of QT ultrasonic waves along the [0001] symmetry direction in a hexagonal crystal of zinc. The focusing has been observed at room temperature. The focusing patterns of the QT modes obtained with various methods are in good agreement with the theory of phonon focusing that is modified to incorporate the effects of finite wave length at ultrasonic frequencies. The calculated epicentral Green's function $\tilde{G}_{33}(\mathbf{x}, t)$ shows a negative square root singularity at the arrival of the focusing SQT rays. This is consistent with the theory of phonon focusing and in excellent agreement with the observed waveform that was obtained with a capillary fracture sound source and a capacitive detector, which shows a very deep minimum at the SQT ray arrival. The diffraction fringes that are observed with the piezoelectric sources are attributable to the interference between collinear QT rays near the conical point.

Acknowledgments

K. Y. Kim and W. Sachse appreciate the financial support from the Physical Acoustics Division of the Office of Naval Research for this work. Use of the facilities of the Materials Science Center at Cornell University is also acknowledged. A. G. Every acknowledges the financial support from the South African Foundation for Research Development and the National Science Council of the Republic of China.

References

1. G. A. Northrop and J. P. Wolfe, in *Nonequilibrium Phonon Dynamics*, ed. E. Bron (Plenum, New York, 1985), p. 165.
2. H. J. Maris, in *Nonequlibrium Phonons in Nonmetallic Crystals*, ed. W. Eisenmenger and A. A. Kaplyanskii (North-Holland, Amsterdam, 1986), p. 51.
3. H. J. Maris, *Phys. Rev.* **B28**, 7033 (1983).
4. A. G. Every, W. Sachse, K. Y. Kim and M. O. Thompson, *Phys. Rev. Lett.* **65**, 1446 (1990).
5. A. G. Every and W. Sachse, *Phys. Rev.* **B28**, 6689 (1991).
6. M. R. Hauser, R. L. Weaver and J. P. Wolfe, *Phys. Rev. Lett.* **68**, 2604 (1992).
7. K. Y. Kim, W. Sachse and A. G. Every, *Phys. Rev. Lett.* **70**, 3443 (1993).
8. R. L. Weaver, M. R. Hauser and J. P. Wolfe, *Z. Phys.* **B90**, 27 (1993).
9. J. Wesner, K. U. Wurz, K. Hilmann and W. Grill, "Imaging of Coherent Phonons", in *Phonon Scattering in Condensed Matter VII*, ed. M. Meissner and R. O. Pohl (Springer-Verlag, Berlin Heidelberg 1992), p. 68.
10. A. A. Kolomenskii and A. A. Maznev, *JETP Lett.* **53**, 423 (1991).
11. K. Y. Kim, A. G. Every and W. Sachse, *J. Acoust. Soc. Am.* **95**, 1942 (1994).
12. K. Y. Kim and W. Sachse, *Phys. Rev.* **B47**, 10993 (1991).
13. M. J. P. Musgrave, *Crystal Acoustics* (Holden-Day, San Francisco, 1970).
14. A. K. McCurdy, *Phys. Rev.* **B9**, 466 (1974).
15. A. G. Every, *Phys. Rev.* **B22**, 1746 (1980).
16. G. F. D. Duff, *Philos. Trans. R. Soc. London* **A252**, 249 (1960).
17. H. J. Maris, *J. Acoust. Soc. Am.* **50**, 812 (1971).

18. F. R. Breckenridge, C. E. Tschiegg and M. Greenspan, *J. Acoust. Soc. Am.* **57**, 626 (1975).
19. A. G. Every and K. Y. Kim, *J. Acoust. Soc. Am.* **95**, 2505 (1994).
20. V. T. Buchwald, *Proc. R. Soc. London* **A253**, 563 (1959).
21. R. Burridge, *Quart. J. Mech. Appl. Math.* **20**, 41 (1967).
22. N. Cameron and G. Eason, *Quart. J. Mech. Appl. Math.* **20**, 23 (1967).
23. F. R. Yeatts, *Phys. Rev.* **B29**, 1674 (1984).
24. A. Tverdokhlebov and J. Rose, *J. Acoust. Soc. Am.* **83**, 118 (1988).
25. V. K. Tewary and C. M. Fortunko, *J. Acoust. Soc. Am.* **91**, 1888 (1992).
26. R. G. Payton, *Elastic Wave Propagation in Transversely Isotropic Media* (Martinus Nijhoff, Hague, 1983).
27. M. G. Cottam and A. A. Maradudin, in *Surface Excitations*, ed. V. M. Agranovich and R. Loudin (Elsevier, Amsterdam, 1984), p. 1.
28. J. H. M. T. van der Hijden, *Propagation of Transient Elastic Waves in Stratified Anisotropic Media* (North Holland, Amsterdam, 1987).
29. A. G. Every, K. Y. Kim and W. Sachse, "Phonon Imaging at Ultrasonic Frequencies: The Dynamic Response of Anisotropic Solids", in *Die Kunst of Phonons*, eds. T. Paszkiewicz and K. Rapcewicz (Plenum, New York, 1994), pp. 66–73.
30. K. Aki and P. G. Richards, *Quantitative Seismology*, Vol. 1 (Freeman, San Francisco, 1980).
31. R. Burridge, P. Chadwick and A. N. Norris, *Proc. Roy. Soc. London* **A440**, 655 (1993).
32. A. G. Every, *Phys. Rev.* **B34**, 2852 (1986).
33. K. Y. Kim, L. Niu, B. Castagnede and W. Sachse, *Rev. Sci. Instrum.* **60**, 2785 (1989).
34. K. Y. Kim and W. Sachse, *J. Appl. Phys.* **75**, 1435 (1994).
35. R. L. Weaver, W. Sachse and K. Y. Kim, "Transient elastic waves in a transversely isotropic plate", MSC Report #7683, Materials Science Center, Cornell University, Ithaca, NY (1993), *J. Appl. Mech*, in press.
36. D. A. Hutchins, in *Physical Acoustics*, **18**, eds. W. P. Mason and R. N. Thurston (Academic, Boston, 1988), p. 21.